# Topological aspects of multi-$k$ antiferromagnetism in cubic rare-earth compounds

(Dated: January 3, 2023)

## Abstract

We advertise rare-earth intermetallics with high-symmetry crystal structures and competing interactions hosting spin structures with non-trivial topological properties as a class of materials amenable for neuromorphic applications. Focussing on the series of cubic $R$Cu compounds, where $R$ = Ho, Er, Tm, the bulk properties of these systems display exceptionally rich magnetic phase diagrams hosting an abundance of different phase pockets characteristic of antiferromagnetic order in the presence of delicately balanced interactions. The electrical transport properties exhibit large anomalous contributions suggestive of topologically nontrivial winding in the electronic and magnetic structures. Neutron diffraction identifies spontaneous long-range magnetic order in terms of commensurate and incommensurate variations of $(\pi\pi 0)$ antiferromagnetism with the possibility for various multi-$\boldsymbol{k}$ configurations supporting topologically nontrivial winding in real and reciprocal space including antiferromagnetic skyrmion lattices. Putatively bringing together different limits of non-trivial topological winding in the same material, the combination of properties promises access to advanced functionalities.

## I. INTRODUCTION

Neuromorphic concepts promise to revolutionize a wide range of different technological platforms[1–3]. In recent years great interest developed in the use of complex magnetic and electronic properties for neuromorphic computing and related applications[4–7]. Complex magnetic modulations with multiple wave vectors, identified in a rapidly growing number of materials, are at the center of these developments. Such magnetic structures are also referred to as magnetic multi-$\boldsymbol{k}$ states—a notion that dates back at least to the 1970s, when it was used to describe the magnetic modulations in materials such as Nd[8] or $CeAl_2$[9]. In large parts, recent discoveries were motivated by the search for topologically nontrivial electronic or magnetic states.

To date, the perhaps most intensively studied class of bulk compounds exhibiting topologically nontrivial order are the cubic chiral magnets crystallizing in space group $P2_13$, namely MnSi, $Fe_xCo_{1-x}Si$, FeGe, $Cu_2OSeO_3$ and related compounds[16]. As illustrated in Fig. 1, a trigonal lattice of skyrmions is observed in a phase pocket in finite magnetic field, associated with a characteristic sixfold-symmetric pattern in small-angle neutron scattering[10]. At low temperatures, the skyrmion lattice may prevail as a metastable state[16], its arrangement may change, and an additional skyrmion state may form independently[17–19]. In recent years, similar magnetic structures have been reported to exist in a wide range of bulk materials. As shown in Figs. 1(b)–1(f), examples include skyrmion lattice order in $GaV_4S_8$[20], $Gd_2PdSi_3$[21], $Gd_3Ru_4Al_{12}$[22], and $GdRu_2Si_2$[11], meron–antimeron lattices in $Co_8Zn_9Mn_3$[12] and CeAlGe[13], monopole–antimonopole lattices in MnGe[14], or fractionalized antiferromagnetic skyrmion lattice in $MnSc_2S_4$[15]. In addition to these bulk materials, topologically nontrivial magnetic textures have also been reported in thin-film systems in which interfacial Dzyaloshinskii–Moriya interactions are important[16].

A simple tool to search for topologically nontrivial properties in the electronic and magnetic structure are non-vanishing Berry phase contributions in the transport properties [23], with the topological Hall effect in the skyrmion lattice of chiral magnets as an early example[24]. In chiral magnets, these phenomena are extremely well understood on the level of mean-field theory. However, emergent transport phenomena are also used as an indicator for topological magnetic order in rare-earth compounds[21,22], requiring careful consideration of the coupling between conduction electrons and rare-earth moments[25]. On a similar note, microscopic studies of the electronic and magnetic order require great care. For instance, when using scattering techniques one of the key experimental tasks concerns discrimination of single-domain multi-$\boldsymbol{k}$ states from multi-domain

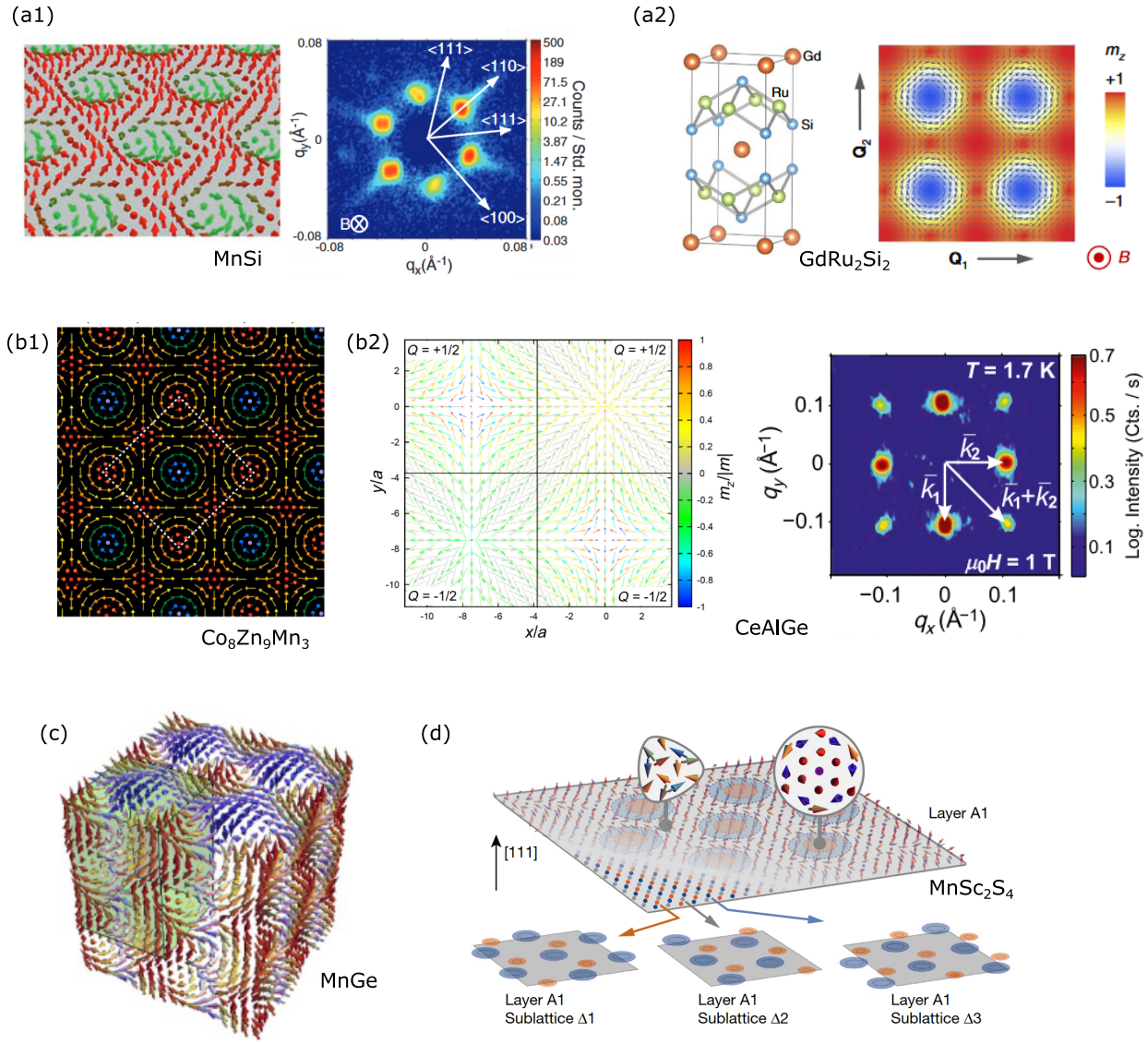


FIG. 1. Survey of materials for which magnetic multi-$\boldsymbol{k}$ states with nontrivial topology have been reported. (a) Trigonal skyrmion lattice in the cubic chiral magnet MnSi. Left: Visualization of the magnetic texture in the plane perpendicular to the magnetic field. Right: Typical small-angle neutron scattering pattern[10]. (b) Nanometric square skyrmion lattice in the centrosymmetric tetragonal magnet $GdRu_2Si_2$. Left: Crystal structure. Right: Arrangement of the magnetic moments in the basal plane[11]. (c) Meron–antimeron lattice in chiral magnet $Co_8Zn_9Mn_3$[12]. (d) Meron–antimeron lattice in the polar tetragonal magnet CeAlGe. Left: Arrangement of the magnetic moments in the basal plane. Right: Typical small-angle neutron scattering pattern[13]. (e) Three-dimensional monopole–antimonopole in cubic MnGe[14]. (f) Fractionalized antiferromagnetic skyrmion lattice in layered $MnSc_2S_4$[15].

TABLE I. Overview of simple cubic rare-earth intermetallics that were reported to host variations of $(\pi\pi 0)$-type magnetic order with propagation vectors associated with the $\boldsymbol{Q}$-positions $(1/2, 1/2, 0)$ or $(1/2-\delta, 1/2, 0)$.

| structure type | commensurate, $\boldsymbol{k} \in \langle 1/2, 1/2, 0\rangle$ | incommensurate, $\boldsymbol{k} \in \{(1/2-\delta, 1/2, 0)\}$ |
|---|---|---|
| CsCl | PrAg[26,27], NdAg[28], TbAg[29], DyAg[30], ErAg[31], GdCu[32], TbCu[29], HoCu[33], TmCu[33], ErCu[33], DyCu | HoAg[34], ErAg[31], TmAg[34], ErCu[33], TmCu[33] |
| $AuCu_3$ | $NdIn_3$[35], $DyIn_3$[36], $TmGa_3$[37], $TbIn_3$[38], $HoIn_3$[38] | $ErGa_3$[39] |

single-$\boldsymbol{k}$ states.

Rare-earth intermetallics with high-symmetric crystal structures represent a class of compounds that was found to exhibit multi-$\boldsymbol{k}$ antiferromagnetic order long ago[40–44], but has so far been mostly ignored when searching for phenomena associated with nontrivial topological winding. In these compounds, partially filled rare-earth $4f$ orbitals typically possess a small overlap resulting in vanishingly small direct exchange[45]. Interactions between the $4f$ moments are instead mediated indirectly via conduction bands and spin-orbit coupling [46–48]. In competition with magnetocrystalline anisotropies and quadrupolar degrees of freedom, rich magnetic phase diagrams emerge supporting various antiferromagnetic forms of order[49–56]. However, these studies predated recent research on the topological properties of magnetic materials motivating to revisit this these systems.

In this paper, we review selected properties of the class of cubic rare-earth copper compounds, *R*Cu (*R* = Gd, Tb, Dy, Ho, Er, Tm) that illustrate the putative existence of non-trivial topological properties in this class of materials, where Tab. I summarizes some of early results on the magnetic structures observed in these systems. Shown in Fig. 2(a) is the centrosymmetric cubic CsCl crystal structure with space group $Pm\bar{3}m$. Below the Néel temperature $T_{\mathrm{N}}$, antiferromagnetic order of the rare-earth moments stabilizes. When increasing the atomic number $Z$ from 64 in gadolinium to 69 in thulium, the Néel temperature decreases by a factor of 20, while the lattice constant $a$ decreases by about 3%, as shown in Fig. 2(b).

Within the parameter range studied, all *R*Cu compounds have been found to exhibit $(\pi\pi 0)$ antiferromagnetic order, comprising long-wavelength commensurate and incommensurate super-

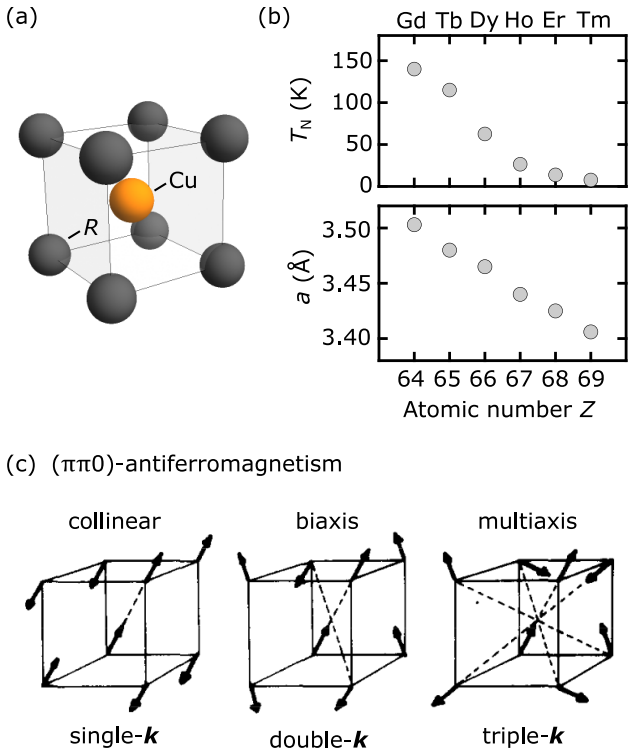


FIG. 2. Overview of the magnetic properties of cubic rare-earth copper compounds *R*Cu. (a) CsCl crystal structure, space-group $Pm\bar{3}m$. (b) Néel temperature $T_N$ (top) and room-temperature lattice constant $a$ (bottom) as a function of the atomic number $Z$ of the rare-earth element. Note that GdCu and TbCu undergo martensitic transitions to orthorombic phases at low temperatures[57]. (c) Illustration of potential $(\pi\pi 0)$ antiferromagnetic order composed of one, two, or three commensurate wave vectors $\boldsymbol{k}$, suggested as possible ground states of HoCu. Panel taken from Ref. 33.

structures around $\boldsymbol{k} \approx (\frac{1}{2}, \frac{1}{2}, 0)$, i.e., the M point of the Brillouin zone. The ground state at low temperatures and zero magnetic field is reported to be commensurate with $\boldsymbol{k} = (1/2, 1/2, 0)$, with single-$\boldsymbol{k}$, double-$\boldsymbol{k}$, or triple-$\boldsymbol{k}$ magnetic structures being allowed in the high-symmetry crystal structure. A triple-$\boldsymbol{k}$ structure was identified for instance in DyCu[58–61], while additional incommensurate log-wavelength superstructures, like those observed reported in TmCu and ErCu, were exclusively considered to be single-$\boldsymbol{k}$.

Our focus review is organized as follows. We begin in Sec. II A with the magnetic phase diagrams of HoCu, ErCu, and TmCu for field along $\langle 111 \rangle$ as inferred from the AC susceptibility. Typical for this class of materials and all field directions, an abundance of field-induced transitions with an exceptionally rich and complex sequence of phase pockets reflects a fragile balance of different interactions comprising exchange, spin-orbit coupling, crystal fields, and f-electron

itineracy. As illustrated for the case of TmCu in Sec. II B, measurements of the electrical transport properties in all of these materials exhibit an anomalous field dependence that does not scale with the magnetization. This is suggestive of non-vanishing Berry phase contributions in real and reciprocal space as presented in Sec. III. Turning to typical neutron single-crystal neutron diffraction data in Sec. III A, we show-case the existence of antiferromagnetic structures combining short-wavelength commensurate order with incommensurate superstructures for the case of HoCu in zero magnetic field. This is followed by a more detailed discussion of the commensurate multi-$\boldsymbol{k}$ states in Sec. III B, which may be viewed in terms of a topological band structure comprising monopoles and antimonopoles in reciprocal space. In comparison, the incommensurate multi-$\boldsymbol{k}$ superstructure, addressed in Sec. III C, may be interpreted in terms of topologically non-trivial, long-wavelength magnetic textures in real-space, such as an antiferromagnetic skyrmion lattice. Our paper concludes in Sec. IV with a summary and a brief outlook of the work program needed to develop a comprehensive understanding of these materials.

## II. BULK PROPERTIES

### A. Magnetic Phase Diagrams

Shown in Fig. 3 are the phase diagrams of HoCu, ErCu, and TmCu under magnetic fields applied parallel to $\langle 111 \rangle$. For the studies mentioned in our paper large single crystals were grown by means of optical float-zoning[62,63]. Depicted in gray shading are interpolation maps of the AC magnetic susceptibility as recorded at an excitation frequency of 911 Hz and an excitation amplitude of 1 mT. Extrema and points of inflection are marked in red. Lines are guides to the eye typically characteristic of phase transitions or crossover phenomena. For lack of space, the AC susceptibility as a function of magnetic field, as well as the magnetization, heat capacity and magnetic phase diagrams for fields along further high-symmetry directions will be reported elsewhere[64–67].

A full microscopic assessment of the magnetic phase diagram based on neutron and x-ray scattering will be required to delineate different phase pockets[67]. Characteristic of a complex antiferromagnetic ground state, the susceptibility on a purely phenomenological level suggests the formation of a large number of phase transitions and cross-over phenomena before the field-polarized regime is reached featuring a uniform, unsaturated magnetization. As a function of

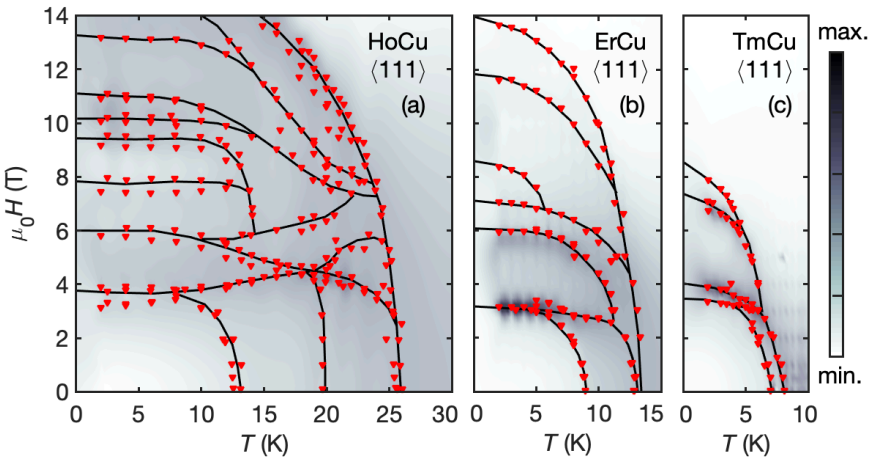


FIG. 3. Magnetic phase diagrams of of HoCu, ErCu, and TmCu for magnetic field $H \parallel \langle 111 \rangle$. Depicted in gray are interpolation maps of the AC magnetic susceptibility $\chi_{\mathrm{AC}}$ recorded for an excitation frequency of 911 Hz and excitation amplitude of 1 mT. Marked in red are maxima and points of inflection observed in the susceptibility. Lines are guides to the eye, suggesting phase transitions or crossover phenomena.

increasing $Z$, i.e., decreasing lattice spacing and single-ion moment when going from Ho to Er to Tm, the onset of the field-polarized state and the ordering temperature $T_{\mathrm{N}}$ decrease. Similarly, the number of magnetic phase pockets appears to decrease across the series. Nonetheless, the mere complexity of the phase diagrams raises the question for the nature of the microscopic magnetic and electronic structure and its possible topological character.

### B. Electrical Transport Properties

The electrical transport properties of the series of RCu compounds, quite generically, display a complex magnetic field dependence[64,67]. Typical behaviour is illustrated best for TmCu, where the comparatively small number of field-induced transitions and the low critical field of the field-polarized state allows direct comparison of the transport properties with the magnetization deep into the field-polarized state. As shown in Fig. 6(a) for $H \parallel \langle 111 \rangle$, corresponding to the phase diagram shown in Fig. 5(c), the magnetization of TmCu at a low temperature of 2 K is dominated by two step-like transitions at $H_1 = 4.0\,\mathrm{T}$ and $H_2 = 6.7\,\mathrm{T}$, before entering the field-polarized state slightly above $H_c = 9.0\,\mathrm{T}$. Further signatures denoted in the phase diagram shown in Fig. 5(c) may only be seen in the AC susceptibility.

In the field-polarized state for $H > H_c$ the resistivity $\rho_{xx}$, shown in Fig. 6(b), increases mono-

tonically with $M(H)$ reminiscent of the transverse magnetoresistance observed in conventional ferromagnets. In comparison, between the transition at $H_1$ and below the onset of the field-polarized state at $H_c$, the resistivity $\rho_{xx}(H)$ displays an additional contribution highlighted in light-blue shading. As this additional contribution may reflect any combination of scattering by the magnetic structure and magnetic textures, as well as changes of the electronic structure, its unambiguous identification is well beyond the scope of our paper.

Similar to the resistivity $\rho_{xx}(H)$, the Hall resistivity $\rho_{xy}(H)$ shown in Fig. 6(c), displays essentially a linear dependence in the field-polarized state above $H_c$. Below $H_c$ a strongly non-monotonic field dependence including a change of sign is observed. Remarkable in its own right is thereby the unusually large quantitative size of these contributions (light-purple shading). It is instructive to asses the Hall resistivity in the conventional way, considering the usual three main contributions, namely

$$\rho_{xy}(H) = R_0\,\mu_0 H + S_A\,\mu_0\,\rho_{xx}^2 M(H) + \Delta\rho_{xy}(H)\,. \tag{1}$$

Here the first term describes the normal Hall effect which is linear under applied magnetic field, while the second term represents the intrinsic anomalous Hall effect which is linear in the magnetization and the resistivity squared. The third term vanishes in the spin-polarized state and is usually attributed to the emergence of additional Berry phase contributions in the presence of magnetic order.

Assuming that the parameter $S_A$ does not change across the complex magnetic phase diagram, the Hall resistivity $\rho_{xy}(H)$ in the field-polarized state is dominated by a normal Hall contribution (NHE) and a small anomalous Hall contribution (AHE) as denoted in Fig. 6(c). In turn, the anomalous contribution in the resistivity $\rho_{xx}$ between $H_1$ and the onset of the field-polarized state at $H_c$ is barely noticeable as compared to the non-monotonic part of the Hall resistivity $\rho_{xy}(H)$. This underscores the putative presence of a combination of different topological contributions in the transport properties and motivates the consideration of the magnetic structure presented in the next section.

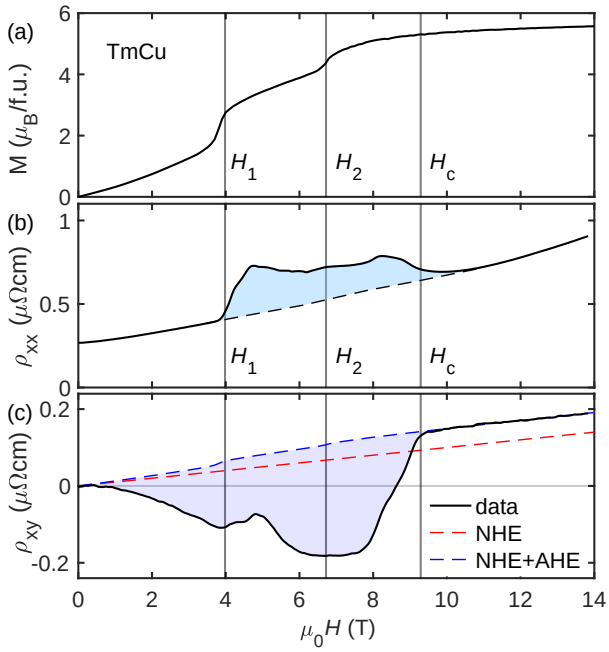


FIG. 4. Magnetization and electrical transport properties of TmCu at $T = 2\,\mathrm{K}$ for magnetic field along $\langle 111 \rangle$. (a) Magnetization as a function of magnetic field, where two dominant step-like transitions at $H_1 = 4.0\,\mathrm{T}$ and $H_2 = 6.7\,\mathrm{T}$ are followed by the onset of the field-polarized state slightly above $H_c = 9.0\,\mathrm{T}$. (b) Electrical resistivity $\rho_{xx}$, featuring a non-monotonic contribution between $H_1$ and $H_c$. (c) Hall resistivity $\rho_{xy}$ of TmCu. Dashed lines represent normal and anomalous Hall contributions denoted NHE and AHE, respectively, as matched to the field polarized state above $H_c$. Shown in light-purple shading is the presence of an exceptionally large non-monotonic signal component in $\rho_{xy}$, providing putative evidence of topological effects.

## III. MAGNETIC STRUCTURE

### A. Typical neutron data

The presentation of typical key characteristics of the magnetic structures in the class of RCu systems may be illustrated best for the case of HoCu at zero field, featuring commensurate short-wavelength antiferromagnetism as well as incommensurate superstructures. For the microscopic determination of the magnetic structures of HoCu, ErCu, and TmCu numerous neutron diffraction experiments at various large-scale facilities were carried out[67–76]. Combining various state-of-the-art methods including spherical neutron polarimetry served to distinguish between arrangements of magnetic moments with equivalent structure factors[77,78], as well as between multi-domain single-

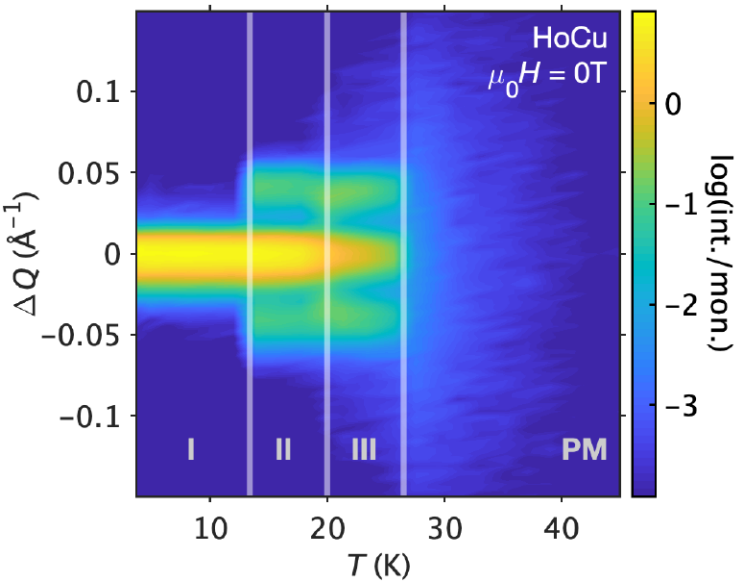


FIG. 5. Magnetic neutron diffraction intensity as a function of temperature in HoCu at zero magnetic field. Three phases denoted I, II and III may be distinguished, reflecting commensurate antiferromagnetism in phase I, with an additional incommensurate superstructure in phases II and III.

$\boldsymbol{k}$ and single-domain multi-$\boldsymbol{k}$ forms of order, tracking higher-order magnetic Bragg components (see also Refs. 79–81).

In the following we illustrate typical behaviour observed in HoCu, ErCu, and TmCu by virtue of the diffraction data recorded in HoCu at zero magnetic field. Data were collected in rocking scans with respect to the reciprocal lattice position $\boldsymbol{Q} = (\frac{3}{2}, \frac{3}{2}, 1) + \Delta\boldsymbol{Q}$ at the single-crystal diffractometer HEiDi at FRM-II[69]. Further results of our neutron diffraction studies will be presented elsewhere[67].

As shown in Fig. 5, the scattering intensity in HoCo at zero magnetic field exhibits three different momentum dependencies with increasing temperature denoted I, II, and III, consistent with the three antiferromagnetic phases observed in the bulk properties. At 2.3 K, the lowest temperatures studied, HoCu displays short-wavelength commensurate $(\pi\pi 0)$ antiferromagnetism with wave-vectors forming a star $\{(1/2, 1/2, 0)\}$, frequently also denoted $\langle 1/2, 1/2, 0\rangle$. Further, at intermediate temperatures when entering phases II and III the scattering intensity is characteristic of incommensurate ordering vectors $\{(1/2 - \delta, 1/2, 0)\}$ with $\delta \approx 0.02$ r.l.u.. These scattering intensities correspond to a long-wavelength superstructure of the short wavelength commensurate antiferromagnetic order observed in phase I.

The incommensurate propagation vectors observed in phases II and III are reminiscent of the

antiferromagnetic order reported in the large class of cubic rare-earth intermetallics summarized in Tab. I. While some of the commensurate states have been considered as candidates of short-wave-length multi-$\boldsymbol{k}$ order, it is interesting to note that the components defining the incommensurate superstructures, $\{(1/2-\delta, 1/2, 0)\}$, may represent long-wavelength multi-$\boldsymbol{k}$ modulated states in their own right. In turn, we limit the discussion of the magnetic structures in HoCu, presented in the following, to phases I and II, since they permit to address the topological character in two opposing limits. Indeed, although in both phases magnetic structure refinements and polarized neutron diffraction may be accounted for by relatively simple collinear forms of antiferromagnetic order, a large set of antiferromagnetic multi-$\boldsymbol{k}$ states with non-trivial topological properties exist some of which may ultimately turn out to be the magnetic ground states.

### B. Phase I of HoCu: Commensurate Order

The magnetic structure in phase I of HoCu corresponds to the irreducible representation $\Gamma_9$ of the M-point in space group $Pm\bar{3}m$[82]. In particular, the magnetic Fourier components propagated by a vector of the star $\langle 1/2, 1/2, 0\rangle$ are restricted to lie within the plane that is perpendicular to the ferromagnetically coupled $\langle 100\rangle$ bond of the respective propagation. The orientation of the corresponding arms $\boldsymbol{k}_{c,1} = (\frac{1}{2}, \frac{1}{2}, 0)$, $\boldsymbol{k}_{c,2} = (0, \frac{1}{2}, \frac{1}{2})$, and $\boldsymbol{k}_{c,3} = (\frac{1}{2}, 0, \frac{1}{2})$, is illustrated in Fig. 7(a), where the magnetic ground state may involve any number of these components.

Presented in Fig. 7(b-d) are examples of single-$\boldsymbol{k}$, double-$\boldsymbol{k}$, and triple-$\boldsymbol{k}$ types of order in excellent agreement with the magnetic structure refinements obtained using JANA2006[83]. Without further constraints, an infinite number of such $\Gamma_9$ structures exists, which cannot be distinguished using unpolarized single-crystal neutron diffraction at zero magnetic field. Careful analysis of neutron diffraction recorded under applied magnetic field, to be presented elsewhere, established finally that structure t1 shown in Fig. 7(d) represents the correct solution of phase I.

In the context of this paper, it is instructive to discuss the properties of t1 in further detail. Namely, the topological properties of the triple-$\boldsymbol{k}$ state t1 cannot emerge from structures with fewer wave vectors. Unlike the single-$\boldsymbol{k}$ state representing a collinear structure, and the double-$\boldsymbol{k}$ state representing a noncollinear coplanar structure, the triple-$\boldsymbol{k}$ state corresponds to a noncoplanar texture of magnetic moments with finite scalar spin chiralities $\sim \boldsymbol{M}_i \cdot (\boldsymbol{M}_j \times \boldsymbol{M}_k)$[84]. As a possible account of electrical transport properties such as those observed in TmCu, such spin chiralities may result in real-space Berry phases and anomalous Hall contributions that are not proportional

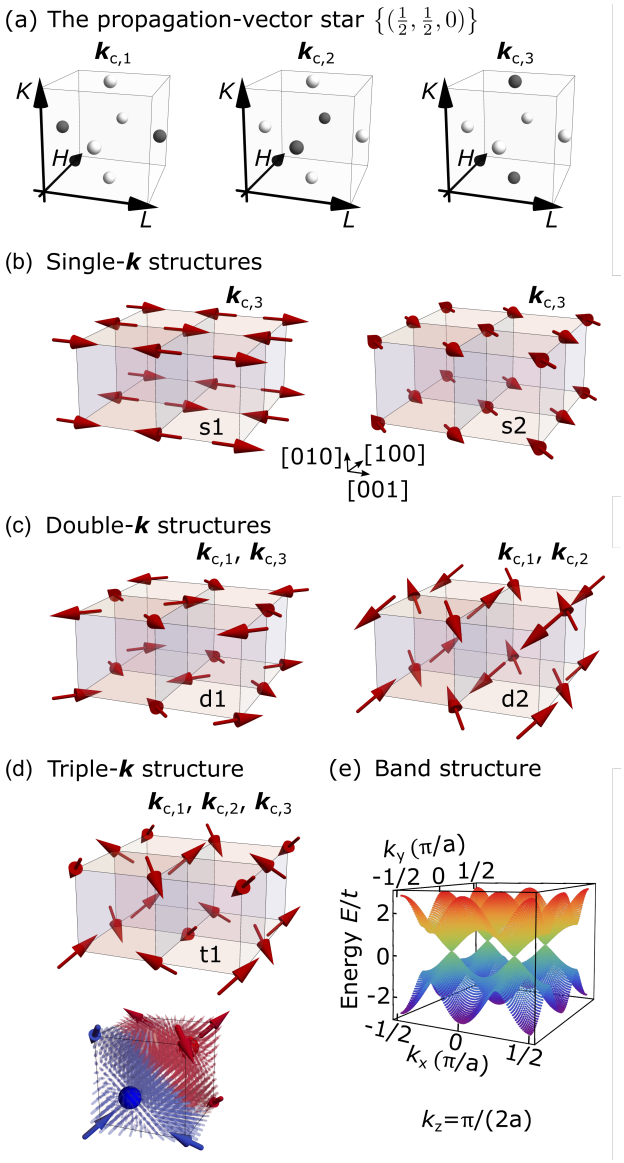


FIG. 6. Magnetic structure of Phase I in HoCu. The magnetic ground state represents a commensurate $(\pi\pi 0)$ antiferromagnet that corresponds to the irreducible representation $\Gamma_9$. (a) Reciprocal space illustration in the Brillouin zone of the three arms of the star of propagation vectors $\langle 1/2, 1/2, 0)\rangle$. In principle, the wave-vectors may form single-$\boldsymbol{k}$, double-$\boldsymbol{k}$, or triple-$\boldsymbol{k}$ structures. (b) to (d) Real space examples of the star of propagation. Measurements under magnetic field establish the structure shown in panel (d) is the solution for phase I of HoCu. Also shown in panel (d) is an extrapolation of the triple-$\boldsymbol{k}$ structure to interatomic positions is illustrated in terms of the directorfield depicted by means of small arrows. One unit cell may be viewed as a monopole–antimonopole pair denoted by a red and a blue sphere at $a(3/4, 3/4, 3/4)$ and $a(1/4, 1/4, 1/4)$, respectively. Colors encode the flux of each arrow with respect to the nearest singularity. (e) Band structure calculated for the triple-$\boldsymbol{k}$ structure in terms of the minimal tight-binding model described in the text.

to the net magnetization $M(H)$[23].

Moreover, the Fourier description of a triple-$\boldsymbol{k}$ ($\pi\pi 0$) state such as t1 is given by

$$\boldsymbol{M}(\boldsymbol{R}) = M_0 \cdot \sum_{i=1}^{3} \hat{m}_i \cdot \cos(\boldsymbol{k}_i \cdot \boldsymbol{R}) \quad , \tag{2}$$

where $\boldsymbol{R}$ denotes the positions of the magnetic rare-earth ions. Decomposing t1 in terms of Fourier components given by $\hat{m_1} = (0,1,0)$, $\hat{m_2} = (0,0,1)$, and $\hat{m_3} = (1,0,0)$, it may be seen that t1 resembles the monopole-antimonopole lattice reported in MnGe[14]. Extending the magnetization $\boldsymbol{M}(\boldsymbol{r})$ analytically to locations between rare-earth lattice sites, singularities are located at the positions $\boldsymbol{r} = \frac{1}{4}(a,a,a)$ and $\frac{3}{4}(a,a,a)$ where the magnetization vanishes and the Berry curvature $\boldsymbol{b_k} = \frac{1}{2} \cdot [\partial_i \boldsymbol{n} \times \partial_j \boldsymbol{n}]$ derived from the directorfield $\boldsymbol{n} = \boldsymbol{M}/|\boldsymbol{M}|$ is topologically non-trivial with effective magnetic charges given by $Q_{\mathrm{M}} = \frac{1}{4\pi} \int_S \mathrm{d}S_{\boldsymbol{k}} \cdot b_{\boldsymbol{k}} = \pm 1$, see Ref. 14. In fact, around the same positions the directorfield forms a hedgehog and an anti-hedgehog, respectively. While a real-space interpretation of phase I based on a continuous magnetization field suggesting microscopic monopoles and anti-monopoles is intriguing, it must also be emphasized that it is inconsistent with a bare magnetic structure, $\boldsymbol{M}(\boldsymbol{R})$, composed of local moments, in which mirror and rotational symmetries must be broken to generate the interpolation $\boldsymbol{M}(\boldsymbol{r})$.

Shedding a different light on the topological properties of the triple-$\boldsymbol{k}$ structure t1, it is instructive to consider the associated band structure on the level of a minimal tight-binding model given by[23]:

$$H = \sum_{\langle i,j \rangle} t_{ij} c_i^\dagger c_j + J_{\mathrm{H}} \sum_i \boldsymbol{\sigma} \cdot \boldsymbol{S}_i c_i^\dagger c_i \quad , \tag{3}$$

where $c_i^\dagger$ and $c_i$ represent the two-component creation and annihilation operators of an electron at site $i$. The first term describes hopping between low-order nearest neighbours and the second term describes the coupling between conduction electrons and the magnetic structure treated as local exchange field $\boldsymbol{S}_i$. In the limit of fully polarized localized moments, i.e., $J_{\mathrm{H}} \to \infty$, a spinless tight-binding model is obtained with hopping parameters $t_{ij}^{\mathrm{eff}} = t_{ij} \cdot \langle \chi_i | \chi_j \rangle$, where

$$|\chi_i\rangle := [\cos(\theta_i/2), \sin(\theta_i/2) \cdot \exp(\mathrm{i} \cdot \Phi_i)]^{\mathrm{T}} \tag{4}$$

represents a spinor describing a classical spin $\boldsymbol{S}_i$ in terms of polar angles $\theta_i$ and $\Phi_i$[23]. Solving this model in the absence of spin–orbit coupling for a typical set of parameters given by $t_{\langle 100 \rangle} = t_{\langle 110 \rangle} = t$, the band structure displays Berry curvature with a rich distribution of positive and negative magnetic charges in reciprocal space[85]. Panel (f) shows the resulting band structure at momentum $k_z = \frac{\pi}{2}$, where four singularities of quantized charges emerge.

The minimal tight-binding model and the resulting assembly of charges creating Berry-curvatures permit to discuss the properties of the triple-$\boldsymbol{k}$ structure t1 further. For instance, in the presence of an anisotropic distortion of the lattice with respect to the [111] direction, a displacement of the charges causing the Berry curvatures are expected resulting in two–dimensional Chern numbers, a finite intrinsic anomalous Hall effect[23], and an orbital magnetization (a similar phenomenon was studied in Ref. 86). The latter may be calculated by means of the expression[87]

$$\mathbf{M}_{\mathrm{orb}} = -\frac{ie}{2\hbar}\sum_{n,\alpha}\int \mathrm{d}^3k\,[\langle\partial_{\mathbf{k}}u_{n,\alpha}|\times(H-E_n)\,|\partial_{\mathbf{k}}u_{n,\alpha}\rangle + \\ +2\,(E_n-E_F)\,\langle\partial_{\mathbf{k}}u_{n,\alpha}|\times|\partial_{\mathbf{k}}u_{n,\alpha}\rangle] \tag{5}$$

where the distortion of the lattice is taken into account in terms of a slight change of hopping parameters for next-nearest neighbour bonds perpendicular to [111]. Finally, for the two domains of the triple-$\boldsymbol{k}$ structure, the orbital magnetization exhibits opposing direction and hance different Zeeman energies under an applied magnetic field. Accordingly, already on the level of this minimal model an anomalous response to an applied magnetic field may be expected.

### C. Phase II of HoCu: Incommensurate Order

The magnetic state associated with phase II of HoCu comprises a combination of commensurate and incommensurate modulations that correspond to the IRs $\Gamma_2$ and $\Gamma_1$ of the wave-vector stars $\langle 1/2, 1/2, 0\rangle$ and $\{(1/2-\delta, 1/2, 0)\}$, respectively. This implies that magnetic moments associated with each wave-vector are directed along the ferromagnetically coupled $\langle 100\rangle$ bond of the respective propagation. The star of incommensurate propagation vectors has six wave-vector arms as illustrated in Fig. 3(a). Since the three arms of commensurate wave-vectors must also be taken into account, the magnetic structure in phase II may be a multi-$\boldsymbol{k}$ structure with up to nine magnetic propagation vectors.

The bare modulation associated with a single incommensurate $\boldsymbol{k}$-vector of the associated IR corresponds to an amplitude modulation, as shown in Fig. 3(b). Such a magnetic state has been reported in HoAg and TmAg[34]. The superposition of such incommensurate wave-vectors with a specific, well-defined phase relation may result in highly non-trival magnetic textures, such as the 4-sublattice non-chiral helix presented in Fig. 3(c). The latter arises from the $\pi/2$-shifted superposition of two amplitude modulations that are incommensurate along the same $\langle 100\rangle$ direction. The simplest possible structure arising from the superposition of commensurate and incommensurate

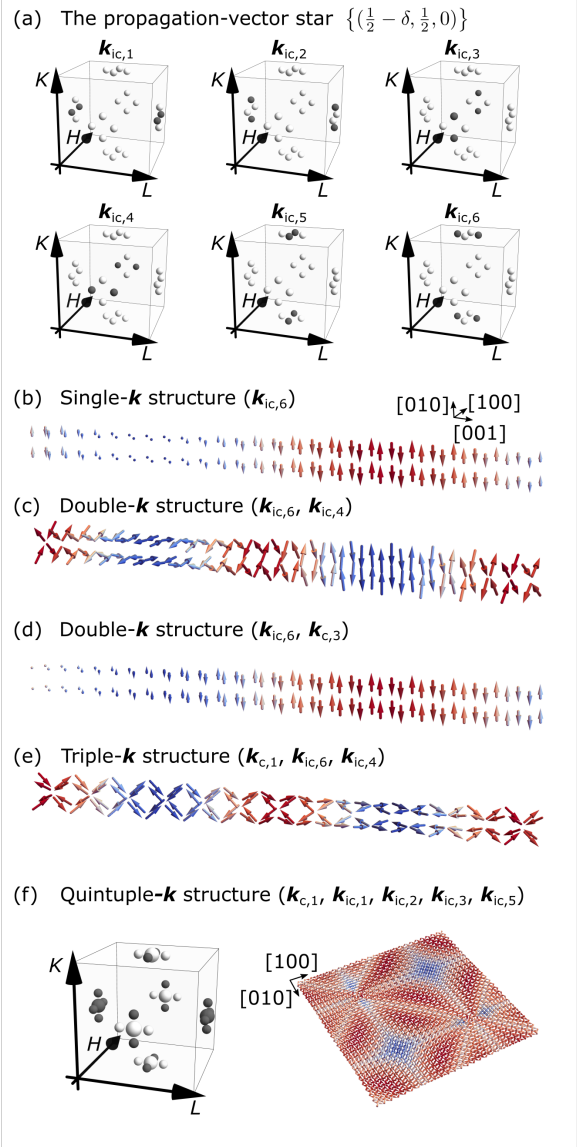


FIG. 7. Magnetic structure determination in Phase II of HoCu. (a) The magnetic ground state is a superposition of wave-vectors from the stars $\{(\frac{1}{2}-\delta,\frac{1}{2},0)\}$ and $\{(\frac{1}{2},\frac{1}{2},0)\}$. The latter yields six arms that are here illustrated by the positions in the Brilloin zone. (b) Bare modulation of a single incommensurate wavevector representing an amplitude modulation. (c) Exemplary phase-shifted superposition of two such amplitude-modulations resulting in a non-chiral helix. (d) Collinear double-$k$ structure resulting from one commensurate and one incommensurate propagation vector. (e) Four-sublattice non-chiral cone-structure resulting from a superposition of two incommensurate and one commensurate propagation vectors and identified by us as the magnetic structure in phase II. (f) Four-sublattice antiferromagnetic skyrmion lattice resulting from a superposition of four incommensurate and one commensurate propagation vectors.

wave-vectors and, according solely to irreducible representations a candidate structure for phase II of HoCu, is the collinear structure shown in Fig. 3(d), which was previously proposed to exist in ErCu and TmCu[33].

Structures with topologically non-trivial properties may emerge when more than one incommensurate modulation are involved. Presented in Fig. 3(e) is the triple-$\boldsymbol{k}$ structure that we identified as the most plausible magnetic solution of phase II. It represents a 4-sublattice antiferromagnetic non-chiral cone. Notably, the latter displays a constant modulus of magnetic moments, which in general is a favourable for $f$-electron moments. The modulation of the real-space texture changes from coplanar to noncoplanar arrangements and the rotation associated with the superstructure follows the parametrization of a staggered parameter making a full winding in the real projective space $\mathbb{R}P^1$ over a real-space distance of $\sim \frac{1}{2} \cdot a/\delta = 9$ nm, which is half of the periodicity of the cones on each sublattice.

Also shown in Fig. 3(f) is a quintuple-$\boldsymbol{k}$ structure, which arises from a superposition of one commensurate and four incommensurate propagation vectors as another possible solution consistent with the irreducible representations of phase II. Illustrated on the left hand side of Fig. 3(f) is the diffraction pattern of a single domain. The associated real-space texture represents a four-sublattice antiferromagnetic skyrmion lattice, in which half of the sublattices display positive winding numbers and the other half negative winding numbers. Starting from this, the superposition of a sufficiently large uniform magnetization as induced by an applied magnetic field may stabilize a four-sublattice skyrmion state with equal winding numbers on each sublattice. The latter may give rise to complex transport properties, such as net Berry phases resulting in transverse resistivity emerging from intra-sublattice conduction processes.

## IV. CONCLUSIONS

In summary, we presented a short review of antiferromagnetic multi-$\boldsymbol{k}$ states in the cubic rare-earth copper compounds with special emphasis of their putative topological character. To illustrate key findings we reported selected results in HoCu, ErCu, and TmCu, representing promising materials that may host topological antiferromagnetic order. In all compounds measurements of the magnetic susceptibility establish multi-pocketed magnetic phase diagrams characteristic of delicately balanced competing interactions. The electrical transport properties exhibit exceptionally large anomalous contributions in the resistivity and Hall effect that are strongly suggestive of non-

trivial topological winding of the electronic and magnetic structure. Neutron scattering reveals variations of $(\pi\pi 0)$ antiferromagnetic order throughout the magnetic phase diagrams, where some of the phases support multi-$\boldsymbol{k}$ states. Focussing on HoCu, we showcased commensurate $(\pi\pi 0)$ order as a platform of a topological band structures comprising monopoles and antimonopoles. On a related note, we predict that incommensurate superstructures of the $(\pi\pi 0)$ antiferromagnetism in phase II of HoCu may provide an example of an antiferromagnetic skyrmion lattice with non-vanishing topological winding in real-space. This combination of properties reflecting opposing limits, connects emerging properties in a unprecedented way, extending the platform of materials properties currently studied in the context of neuromorphic applications[1–4,6,7].

---


[1] D. V. Christensen, R. Dittmann, B. Linares-Barranco, A. Sebastian, M. Le Gallo, A. Redaelli, S. Slesazeck, T. Mikolajick, S. Spiga, S. Menzel, I. Valov, G. Milano, C. Ricciardi, S.-J. Liang, F. Miao, M. Lanza, T. J. Quill, S. T. Keene, A. Salleo, J. Grollier, D. Marković, A. Mizrahi, P. Yao, J. J. Yang, G. Indiveri, J. P. Strachan, S. Datta, E. Vianello, A. Valentian, J. Feldmann, X. Li, W. H. P. Pernice, H. Bhaskaran, S. Furber, E. Neftci, F. Scherr, W. Maass, S. Ramaswamy, J. Tapson, P. Panda, Y. Kim, G. Tanaka, S. Thorpe, C. Bartolozzi, T. A. Cleland, C. Posch, S. Liu, G. Panuccio, M. Mahmud, A. N. Mazumder, M. Hosseini, T. Mohsenin, E. Donati, S. Tolu, R. Galeazzi, M. E. Christensen, S. Holm, D. Ielmini, and N. Pryds, "2022 roadmap on neuromorphic computing and engineering," Neuromorph. Comput. Eng. **2**, 022501 (2022).

[2] P. K. Singh, Y. Singh, J. K. Chhabra, Z. Illés, and C. Verma, eds., *Recent Innovations in Computing: Proceedings of ICRIC 2021, Volume 2*, Vol. 855 (Springer Singapore, 2022).

[3] D. Marković, A. Mizrahi, D. Querlioz, and J. Grollier, "Physics for neuromorphic computing," Nat Rev Phys **2**, 499 (2020).

[4] J. Grollier, D. Querlioz, K. Y. Camsari, K. Everschor-Sitte, S. Fukami, and M. D. Stiles, "Neuromorphic spintronics," Nat Electron **3**, 360 (2020).

[5] K. M. Song, J.-S. Jeong, B. Pan, X. Zhang, J. Xia, S. Cha, T.-E. Park, K. Kim, S. Finizio, J. Raabe, J. Chang, Y. Zhou, W. Zhao, W. Kang, H. Ju, and S. Woo, "Skyrmion-based artificial synapses for neuromorphic computing," Nat Electron **3**, 148 (2020).

[6] A. Mahmoud, F. Ciubotaru, F. Vanderveken, A. V. Chumak, S. Hamdioui, C. Adelmann, and S. Cotofana, "Introduction to spin wave computing," Journal of Applied Physics **128**, 161101 (2020).

[7] A. Hoffmann, S. Ramanathan, J. Grollier, A. D. Kent, M. Rozenberg, I. K. Schuller, O. Shpyrko, R. Dynes, Y. Fainman, A. Frano, E. E. Fullerton, G. Galli, V. Lomakin, S. P. Ong, A. K. Petford-Long, J. A. Schuller, M. D. Stiles, Y. Takamura, and Y. Zhu, "Quantum materials for energy-efficient neuromorphic computing," APL Materials **10**, 070904 (2022), arXiv:2204.01832 [cond-mat, physics:physics].

[8] P. Bak and B. Lebech, ""Triple-$\vec{q}$" Modulated Magnetic Structure and Critical Behavior of Neodymium," Phys. Rev. Lett. **40**, 800 (1978).

[9] S. M. Shapiro, E. Gurewitz, R. D. Parks, and L. C. Kupferberg, "Multiple-$q$ Magnetic Structure in $CeaI_2$," Phys. Rev. Lett. **43**, 1748 (1979).

[10] S. Mühlbauer, B. Binz, F. Jonietz, C. Pfleiderer, A. Rosch, A. Neubauer, R. Georgii, and P. Böni, "Skyrmion Lattice in a Chiral Magnet," Science **323**, 915–919 (2009).

[11] N. D. Khanh, T. Nakajima, X. Yu, S. Gao, K. Shibata, M. Hirschberger, Y. Yamasaki, H. Sagayama, H. Nakao, L. Peng, K. Nakajima, R. Takagi, T.-hisa Arima, Y. Tokura, and S. Seki, "Nanometric square skyrmion lattice in a centrosymmetric tetragonal magnet," Nat. Nanotechnol. **15**, 444 (2020).

[12] X. Z. Yu, W. Koshibae, Y. Tokunaga, K. Shibata, Y. Taguchi, N. Nagaosa, and Y. Tokura, "Transformation between meron and skyrmion topological spin textures in a chiral magnet," Nature **564**, 95 (2018).

[13] P. Puphal, V. Pomjakushin, N. Kanazawa, V. Ukleev, D. J. Gawryluk, J. Ma, M. Naamneh, N. C. Plumb, L. Keller, R. Cubitt, E. Pomjakushina, and J. S. White, "Topological Magnetic Phase in the Candidate Weyl Semimetal CeAlGe," Phys. Rev. Lett. **124**, 017202 (2020).

[14] N. Kanazawa, Y. Nii, X.-X. Zhang, A. S. Mishchenko, G. De Filippis, F. Kagawa, Y. Iwasa, N. Nagaosa, and Y. Tokura, "Critical phenomena of emergent magnetic monopoles in a chiral magnet," Nat. Commun. **7**, 11622 (2016).

[15] S. Gao, H. D. Rosales, F. A. Gómez Albarracín, V. Tsurkan, G. Kaur, T. Fennell, P. Steffens, M. Boehm, P. Čermák, A. Schneidewind, E. Ressouche, D. C. Cabra, C. Rüegg, and O. Zaharko, "Fractional antiferromagnetic skyrmion lattice induced by anisotropic couplings," Nature **586**, 37 (2020).

[16] C. Back, V. Cros, H. Ebert, K. Everschor-Sitte, A. Fert, M. Garst, T. Ma, S. Mankovsky, T. L. Monchesky, M. Mostovoy, N. Nagaosa, S. S. P. Parkin, C. Pfleiderer, N. Reyren, A. Rosch, Y. Taguchi, Y. Tokura, K. von Bergmann, and J. Zang, "The 2020 skyrmionics roadmap," J. Phys. D: Appl. Phys. **53**, 363001 (2020).

[17] A. Chacon, L. Heinen, M. Halder, A. Bauer, W. Simeth, S. Mühlbauer, H. Berger, M. Garst, A. Rosch, and C. Pfleiderer, "Observation of two independent skyrmion phases in a chiral magnetic material," Nature Physics **14**, 936 (2018).

[18] M. Halder, A. Chacon, A. Bauer, W. Simeth, S. Mühlbauer, H. Berger, L. Heinen, M. Garst, A. Rosch, and C. Pfleiderer, "Thermodynamic evidence of a second skyrmion lattice phase and tilted conical phase in $cu_2oseo_3$," Phys. Rev. B **98**, 144429 (2018).

[19] A. Aqeel, J. Sahliger, T. Taniguchi, S. Mändl, D. Mettus, H. Berger, A. Bauer, M. Garst, C. Pfleiderer, and C. H. Back, "Microwave Spectroscopy of the Low-Temperature Skyrmion State in Cu 2 OSeO 3," Phys. Rev. Lett. **126**, 017202 (2021).

[20] I. Kezsmarki, S. Bordacs, P. Milde, E. Neuber, L. M. Eng, J. S. White, H. M. Ronnow, C. D. Dewhurst, M. Mochizuki, K. Yanai, H. Nakamura, D. Ehlers, V. Tsurkan, and A. Loidl, "Néel-type skyrmion lattice with confined orientation in the polar magnetic semiconductor $GaV_4S_8$," Nat. Mater **14**, 1116 (2015).

[21] T. Kurumaji, T. Nakajima, M. Hirschberger, A. Kikkawa, Y. Yamasaki, H. Sagayama, H. Nakao, Y. Taguchi, T.-hisa Arima, and Y. Tokura, "Skyrmion lattice with a giant topological Hall effect in a frustrated triangular-lattice magnet," Science **365**, 914 (2019).

[22] M. Hirschberger, T. Nakajima, S. Gao, L. Peng, A. Kikkawa, T. Kurumaji, M. Kriener, Y. Yamasaki, H. Sagayama, H. Nakao, K. Ohishi, K. Kakurai, Y. Taguchi, X. Yu, T.-hisa Arima, and Y. Tokura, "Skyrmion phase and competing magnetic orders on a breathing kagomé lattice," Nat. Commun. **10**, 5831 (2019).

[23] N. Nagaosa, J. Sinova, S. Onoda, A. H. MacDonald, and N. P. Ong, "Anomalous Hall effect," Rev. Mod. Phys. **82**, 1539 (2010).

[24] A. Neubauer, C. Pfleiderer, B. Binz, A. Rosch, R. Ritz, P. G. Niklowitz, and P. Böni, "Topological Hall Effect in the *a* Phase of MnSi," Phys. Rev. Lett. **102**, 186602 (2009).

[25] Y. Yasui, C. J. Butler, N. D. Khanh, S. Hayami, T. Nomoto, T. Hanaguri, Y. Motome, R. Arita, T.-hisa Arima, Y. Tokura, and S. Seki, "Imaging the coupling between itinerant electrons and localised moments in the centrosymmetric skyrmion magnet GdRu2Si2," Nat Commun **11**, 5925 (2020).

[26] P. Morin and D. Schmitt, "Magnetic properties and quadrupolar interactions in PrAg," Phys. Rev. B **26**, 3891 (1982).

[27] D. Givord, P. Morin, and D. Schmitt, "Study of antiferromagnetic structures by polarized neutrons: Application to PrAg," J. Appl. Phys. **57**, 2127 (1985).

[28] K. H. J. Buschow, J. P. de Jong, H. W. Zandbergen, and B. van Laar, "Magnetic properties of some light rare-earth compounds with CsCl structure," J. Appl. Phys. **46**, 1352 (1975).

[29] J. W. Cable, W. C. Koehler, and E. O. Wollan, "Magnetic Order in Rare-Earth Intermetallic Compounds," Phys. Rev. **136**, A240 (1964).

[30] G. Arnold, N. Nereson, and C. Olsen, "Magnetic Structure of DyAg," J. Chem. Phys. **46**, 4041 (1967).

[31] N. Nereson, "Magnetic properties of ErAg," J. Appl. Phys. **44**, 4727 (1973).

[32] J. A. Blanco, J. I. Espeso, J. García Soldevilla, J. C. Gómez Sal, M. R. Ibarra, C. Marquina, and H. E. Fischer, "Magnetic structure of GdCu through the martensitic structural transformation: A neutron-diffraction study," Phys. Rev. B **59**, 512 (1999).

[33] P. Morin and D. Schmitt, "Competition between multi-q antiferromagnetic structures in cubic rare earth-copper compounds," Journal of Magnetism and Magnetic Materials **21**, 243 (1980).

[34] P. Morin, D. Schmitt, and C. Vettier, "Squaring-up of modulated magnetic structures in HoAg and TmAg," J. Phys. France **46**, 39 (1985).

[35] M. Amara, R. M. Galéra, P. Morin, J. Voiron, and P. Burlet, "Magnetic phase diagram in NdIn3 antiferromagnet," Journal of Magnetism and Magnetic Materials **131**, 402 (1994).

[36] "The interplay of the crystalline electric field and quadrupolar interactions in the spontaneous magnetic phases of $DyIn_3$," .

[37] P. Morin, M. Giraud, P. Burlet, and A. Czopnik, "Antiferroquadrupolar and antiferromagnetic structures in TmGa3," Journal of Magnetism and Magnetic Materials **68**, 107 (1987).

[38] N. Nereson and G. Arnold, "Magnetic Properties of TbIn3, TbPt3 and HoIn3," J. Chem. Phys. **53**, 2818 (1970).

[39] A. Murasik, A. Czopnik, L. Keller, and P. Fischer, "Spin rotation in ErGa3," Journal of Magnetism and Magnetic Materials **213**, 101 (2000).

[40] K. Buschow, "Intermetallic compounds of rare-earth and 3d transition metals," Rep. Prog. Phys. **40**, 1179 (1977).

[41] K. Buschow, "Intermetallic compounds of rare earths and non-magnetic metals," Rep. Prog. Phys. **42**, 1373 (1979).

[42] J. Rossat-Mignod, "Magnetic structures of rare earth intermetallics," J. Phys. Colloques **40**, C5 (1979).

[43] A. Szytuła and J. Leciejewicz, "Chapter 83 Magnetic properties of ternary intermetallic compounds of the RT2X2 type," in *Handbook on the Physics and Chemistry of Rare Earths*, Vol. 12 (Elsevier, 1989) p. 133.

[44] D. Gignoux and D. Schmitt, "Chapter 2 Magnetism of compounds of rare earths with non-magnetic metals," in *Handbook of Magnetic Materials*, Vol. 10 (Elsevier, 1997) p. 239.

[45] Jens Jensen and Allan R Mackintosh, *Rare earth magnetism* (Clarendon Oxford, 1991).

[46] M. A. Ruderman and C. Kittel, "Indirect Exchange Coupling of Nuclear Magnetic Moments by Conduction Electrons," Phys. Rev. **96**, 99 (1954).

[47] T. Kasuya, "A Theory of Metallic Ferro- and Antiferromagnetism on Zener's Model," Progress of Theoretical Physics **16**, 45 (1956).

[48] K. Yosida, "Magnetic Properties of Cu-Mn Alloys," Phys. Rev. **106**, 893 (1957).

[49] R. M. G. ra, E. Sole, M. Amara, P. Morin, P. Burlet, and A. P. Murani, "The interplay of the crystalline electric field and quadrupolar interactions in the spontaneous magnetic phases of DyIn3," J. Phys.: Condens. Matter **15**, 6269 (2003).

[50] I. Kakeya, T. Kakeshita, K. Kindo, Y. Yamamoto, and T. Saburi, "High Field Magnetization in DyCu," J. Phys. Soc. Jpn. **68**, 1025 (1999).

[51] M. Amara, P. Morin, and F. Bourdarot, "Experimental study of the magnetic phase diagrams of DyCu," J. Phys.: Condens. Matter **9**, 7441 (1997).

[52] M. Amara, P. Morin, and P. Burlet, "Experimental study of the magnetic phase diagrams in NdZn," Physica B: Condensed Matter **210**, 157 (1995).

[53] "Magnetic phase diagram in $NdIn_3$," .

[54] P. Morin, J. Rouchy, K. Yonenobu, A. Yamagishi, and M. Date, "Interplay of antiferromagnetic and antiferroquadrupolar interactions in DyAg and other rare earth intermetallic compounds," Journal of Magnetism and Magnetic Materials **81**, 247 (1989).

[55] P. Morin, M. Giraud, P. Burlet, and A. Czopnik, "Antiferroquadrupolar and antiferromagnetic structures in TmGa3," Journal of Magnetism and Magnetic Materials **68**, 107 (1987).

[56] J. Rossat-Mignod, P. Burlet, J. Villain, H. Bartholin, W. Tcheng-Si, D. Florence, and O. Vogt, "Phase diagram and magnetic structures of CeSb," Phys. Rev. B **16**, 440 (1977).

[57] P. Morin and D. Schmitt, "Chapter 1 Quadrupolar interactions and magneto-elastic effects in rare earth intermetallic compounds," in *Handbook of Ferromagnetic Materials*, Vol. 5 (Elsevier, 1990) p. 1.

[58] R. Aléonard, P. Morin, and J. Rouchy, "Magnetic and quadrupolar properties of DyCu and related dysprosium cubic compounds," Journal of Magnetism and Magnetic Materials **46**, 233 (1984).

[59] I. Kakeya, T. Kakeshita, K. Kindo, Y. Yamamoto, and T. Saburi, "High Field Magnetization in DyCu," J. Phys. Soc. Jpn. **68**, 1025 (1999).

[60] M. Yasui, T. Terai, T. Kakeshita, M. Matsuda, N. Metoki, and H. Nojiri, "Neutron diffraction study of magnetic structure in DyCu under magnetic field," J. Appl. Phys. **103**, 07B710 (2008).

[61] M. Amara, P. Morin, and F. Bourdarot, "Experimental study of the magnetic phase diagrams of DyCu," J. Phys.: Condens. Matter **9**, 7441 (1997).

[62] A. Neubauer, J. Bœuf, A. Bauer, B. Russ, H.v. Löhneysen, and C. Pfleiderer, "Ultra-high vacuum compatible image furnace," Rev. Sci. Instrum. **82**, 013902 (2011).

[63] A. Bauer, G. Benka, A. Regnat, C. Franz, and C. Pfleiderer, "Ultra-high vacuum compatible preparation chain for intermetallic compounds," Rev. Sci. Instrum. **87**, 113902 (2016).

[64] Marein Rahn, *Search for topological properties of multi-k magnetic structures*, Diploma thesis, Technical University of Munich (2013), unpublished.

[65] Hubert Hautmann, *Untersuchung des magnetischen Phasendiagramms von ErCu*, Bachelor thesis, Technical University of Munich (2013), unpublished.

[66] Nives Bonacic, *Measurements of heat capacity of systems with complex magnetic phase diagrams for magnetic field along hard magnetisation axis*, Master thesis, University of Zagreb (2016), thesis carried out in the group of C. Pfleiderer at the Technical University of Munich.

[67] Wolfgang Simeth, *Investigation of antiferromagnetic superstructures in rare-earth compounds*, Phd thesis, Technical University of Munich (2019).

[68] Y. Su, K. Nemkovskiy, and S. Demirdiş, "DNS: Diffuse scattering neutron time-of-flight spectrometer," J. Large-Scale Res. Facil. JLSRF **1**, 27 (2015).

[69] M. Meven and A. Sazonov, "HEiDi: Single crystal diffractometer at hot source," J. Large-Scale Res. Facil. JLSRF **1** (2015), 10.17815/jlsrf-1-20.

[70] R. Georgii, T. Weber, G. Brandl, M. Skoulatos, M. Janoschek, S. Mühlbauer, C. Pfleiderer, and P. Böni, "The multi-purpose three-axis spectrometer (TAS) MIRA at FRM II," Nucl. Instrum. Methods Phys. Res. Sect. Accel. Spectrometers Detect. Assoc. Equip. **881**, 60 (2018).

[71] L. C. Chapon, P. Manuel, P. G. Radaelli, C. Benson, L. Perrott, S. Ansell, N. J. Rhodes, D. Raspino, D. Duxbury, E. Spill, and J. Norris, "Wish: The New Powder and Single Crystal Magnetic Diffractometer on the Second Target Station," Neutron News **22**, 22 (2011).

[72] A. Ostermann and T. Schrader, "BIODIFF: Diffractometer for large unit cells," J. Large-Scale Res. Facil. JLSRF **1**, 2 (2015).

[73] A. Heinemann and S. Mühlbauer, "SANS-1: Small angle neutron scattering," J. Large-Scale Res. Facil. JLSRF **1**, 10 (2015).

[74] D. A. Keen, M. J. Gutmann, and C. C. Wilson, "SXD – the single-crystal diffractometer at the ISIS spallation neutron source," J Appl Cryst, J Appl Crystallogr **39**, 714 (2006).

[75] K. Prokes and F. Yokoachiya, "E4: The 2-Axis Diffractometer at BER II," J. Large-Scale Res. Facil. JLSRF **3**, 104 (2017).

[76] V. Hutanu, "POLI: Polarised hot neutron diffractometer," J. Large-Scale Res. Facil. JLSRF **1**, 16 (2015).

[77] Y.-Y. Li, "Magnetic Moment Arrangements and Magnetocrystalline Deformations in Antiferromagnetic Compounds," Phys. Rev. **100**, 627 (1955).

[78] G. Shirane, "A note on the magnetic intensities of powder neutron diffraction," Acta Cryst **12**, 282 (1959).

[79] B. Barbara, M. F. Rossignol, J. X. Boucherle, and C. Vettier, "Multiple-$\vec{\mathrm{q}}$ Structure or Coexistence of Different Magnetic Phases in $Ceal_2$?" Phys. Rev. Lett. **45**, 938 (1980).

[80] E. M. Forgan, E. P. Gibbons, K. A. McEwen, and D. Fort, "Observation of a Quadruple-$q$ Magnetic Structure in Neodymium," Phys. Rev. Lett. **62**, 470 (1989).

[81] T. Adams, S. Mühlbauer, C. Pfleiderer, F. Jonietz, A. Bauer, A. Neubauer, R. Georgii, P. Böni, U. Keiderling, K. Everschor, M. Garst, and A. Rosch, "Long-Range Crystalline Nature of the Skyrmion Lattice in MnSi," Phys. Rev. Lett. **107**, 217206 (2011).

[82] A. S. Wills, "A new protocol for the determination of magnetic structures using simulated annealing and representational analysis (SARAh)," Physica B: Condensed Matter **276-278**, 680 (2000).

[83] V. Petříček, M. Dušek, and L. Palatinus, "Crystallographic Computing System JANA2006: General features," Z. Für Krist. - Cryst. Mater. **229** (2014), 10.1515/zkri-2014-1737.

[84] H. Ishizuka and N. Nagaosa, "Spin chirality induced skew scattering and anomalous Hall effect in chiral magnets," Sci. Adv. **4**, eaap9962 (2018).

[85] D. Xiao, J. Shi, and Q. Niu, "Berry Phase Correction to Electron Density of States in Solids," Phys. Rev. Lett. **95**, 137204 (2005).

[86] R. Shindou and N. Nagaosa, "Orbital Ferromagnetism and Anomalous Hall Effect in Antiferromagnets on the Distorted fcc Lattice," Phys. Rev. Lett. **87**, 116801 (2001).

[87] J. Shi, G. Vignale, D. Xiao, and Q. Niu, "Quantum Theory of Orbital Magnetization and Its Generalization to Interacting Systems," Phys. Rev. Lett. **99**, 197202 (2007).